Resolution Enhancement of Multi-look Imagery for the Multispectral Thermal Imager

Amy Galbraith, James Theiler, Kurtis Thome, and Richard Ziolkowski

***Abstract*— This paper studies the feasibility of enhancing the spatial resolution of multi-look Multispectral Thermal Imager (MTI) imagery using an iterative resolution enhancement algorithm known as Projection Onto Convex Sets (POCS). A multi-angle satellite image modeling tool is implemented, and simulated multi-look MTI imagery is formed to test the resolution enhancement algorithm. Experiments are done to determine the optimal configuration and number of multi-angle low-resolution images needed for a quantitative improvement in the spatial resolution of the high-resolution estimate. The issues of atmospheric path radiance and directional reflectance variations are explored to determine their effect on the resolution enhancement performance.**

I. Introduction

The need for higher spatial resolution in remote sensing has led to dramatic improvements in imaging technology over the last three decades. New commercial satellites such as IKONOS [1] and Quickbird [2] have ground resolution finer than one meter. Many customers of remote sensing imagery demand the highest spatial-resolution images that are available. Urban planning, military planning, intelligence, and disaster monitoring/evaluation are several tasks in which very high spatial resolution is needed. The objects of interest for these tasks are often small compared to the ground resolution of satellite-based sensors.

There are several trade-offs to consider pertaining to spatial resolution of satellites. Size and weight limitations of the satellite leads to a problem of attaining higher spatial resolutions. Telescopes, for example, become more powerful as the lens or light-focusing mirror gets larger; the Hubble telescope had to fit within the Space Shuttle cargo bay, fundamentally limiting its resolution. For multispectral sensors, there is a tradeoff between spectral and spatial resolution when designing a system. Multispectral systems often require multiple detector arrays, one for each spectral band, which are expensive; by lowering the spatial resolution of each detector, more bands may be put on the sensor for the same cost. Another difficulty is the storage and processing of high-resolution imagery. While desiring higher and higher resolution imagery, more and more storage and processing time are needed to handle the increased file sizes.

An alternative way to increase image resolution is to design the sensor system to acquire images at a lower resolution and use the sensor system's pointing capabilities to allow collection of multiple low-resolution images within a short time span as the sensor travels over a target area. Then, image processing methods to fuse the multiple low-resolution images into a single high resolution image may be used [3–5]. However, applying these resolution enhancement algorithms to satellite imagery acquired by rapid pointing maneuvers adds considerable complexity to the problem. The images have geometric distortions due to different satellite view angles, have a variable ground resolution cell size [6] due to the changing optical path length from the sensor to the ground at different view angles, and are affected by atmospheric conditions and directional reflectance effects from surface materials.

Several satellite-based imaging systems have the ability to quickly acquire images at different view angles. These include the Multispectral Thermal Imager (MTI) [7, 8], IKONOS [1], Quickbird [2], the Multi-angle Imaging Spectro-Radiometer (MISR) [9], the Along Track Scanning Radiometers (ATSR-1, ATSR-2, AATSR) [10], and the Compact High Resolution Imaging Spectrometer (CHRIS) [11]. The "agility" of a pointable spacecraft varies from platform to platform, limiting the number of images that may be imaged in a single pass over a ground target. For instance, the MTI instrument was designed to acquire two images of a tasked ground target, while the CHRIS instrument on the Project For On-Board Autonomy (PROBA) mission is capable of collecting five images on a single overpass [12]. The MISR instrument collects nine images, but does so by using nine cameras at fixed angles rather than pointing a single camera. The maximum number of images that a particular sensor is capable of collecting during an overpass depends on many factors including the slew rate of the platform under constraints of maximal torque, the amount of on-board memory, data transfer rates, attitude control procedures, and other overhead processing.

This paper studies the feasibility of enhancement of data from the MTI, which acquires two images for each scene of interest. The goal of the work is the creation of a single high-resolution image from multiple low-resolution images taken at different look angles. Several processing steps are used to combine multi-angle images into a single high resolution image, as shown in Fig. 1. Each image, or "frame," may be optionally pre-processed to compensate for atmospheric and BRDF effects. Then, the frames are aligned with each other, or registered [13]. The co-registered, corrected frames are then input to a resolution enhancement algorithm that synthesizes a high resolution image.

A. Galbraith and J. Theiler are with the Los Alamos National Laboratory, Los Alamos, NM, 87545 USA. K. Thome is with the Optical Sciences Center, The University of Arizona, Tucson, AZ 85721 USA. R. Ziolkowski is with the Department of Electrical and Computer Engineering, The University of Arizona, Tucson, AZ 85721 USA.

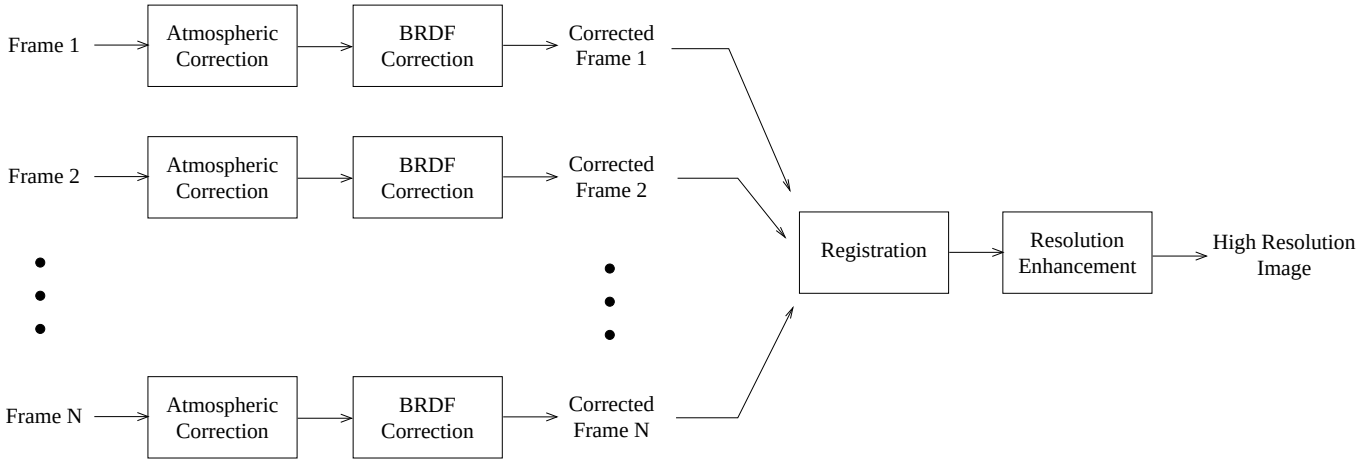

Fig. 1. Flow diagram of resolution enhancement processing for multi-angle remotely-sensed imagery.

II. Multispectral Thermal Imager: MTI

The Multispectral Thermal Imager (MTI) is a U.S. Department of Energy research satellite with fifteen spectral bands, from the visible to the thermal infrared [7, 8]. The MTI platform is a pushbroom system. For near-nadir images, the ground resolution cell size (hereafter called "resolution" for simplicity) is approximately 5 meters for the visible and the near-infrared bands (bands A through D), and 20 meters for the midwave and the thermal bands (bands E through O). The focal plane contains three sensor chip assemblies (SCAs), each consisting of linear detector arrays for each band. The purpose of multiple SCAs is to increase the crosstrack field of view (nominally 12 km). The line detectors for the visible and near infrared (VNIR) bands are located near the center of the focal plane where the optical quality is highest. Each line detector has a delayed start time for readout, so that the 48 images (3 SCAs, 16 line detectors each) are collected sequentially in time, about 4.5 seconds for all of the bands to acquire a 12 km by 12 km image [14].

To increase the system's image acquisition flexibility, the MTI satellite has pointing capabilities, meaning that an image can be taken off to a side, forward, or behind at a given *look angle*. Pointing allows the MTI to acquire a *two-look* image. First, an image is taken with the camera pointing (almost) straight down at a target on the Earth's surface. This image is called the *nadir* image. The target is usually located some distance away from the satellite's orbital track in the cross-track direction, so the nadir image look angle is not exactly zero; rather, it is as close to a nadir angle as is possible given the current orbital position of the satellite, but at least within 20 degrees of nadir. After the satellite has continued in its orbit for a short time, on the order of a few minutes, it then points back at the first target location and acquires a second, *off-nadir* image. The off-nadir image is taken with a look angle of 50 to 60 degrees, typically. The number of images that may be taken in a single overpass is limited by the time required to reorient the satellite. In theory, more images could be taken, but this has not been done during MTI collects. The cross-track pointing has a range of ± 20 degrees, and the along-track pointing has a range of ± 60 degrees. With an orbit height of 575 km and a satellite speed of 7 km/sec, the MTI has a little under 5 minutes in which it must point at and acquire its target scene.

The spatial resolution of the off-nadir image is poorer than that of the nadir image because the extent of the projection of a detector onto the ground, or resolution, is a factor of $\cos^2\theta$ larger, as shown in Fig. 2. The off-nadir resolution in the along-track direction is given by

$$\mathrm{RES}_\theta = \frac{\beta h}{\cos^2\theta} = \frac{\mathrm{RES}_n}{\cos^2\theta} \tag{1}$$

where RES_n is the nadir ground resolution, θ is the angle from nadir, β is the angular instantaneous field of view (IFOV), and h is the distance from the sensor to the ground [6, 15]. This simplified diagram does not account for satellite motion or the detector integration time, which increase the nadir and the off-nadir along-track resolution. The cross-track resolution is similar to the along-track resolution, but scales by $\cos\theta$ rather than $\cos^2\theta$, resulting in an oblong projection of each pixel onto the ground. For the 12 km swath width of MTI, the cross-track resolution is approximately constant.

III. Goal of Resolution Enhancement

Given a set of low resolution images, the goal of resolution enhancement is to form a single image with higher resolution, so that the effective ground resolution cell size is improved. Improving the resolution by combining data from several images will allow finer detail to be seen in the image by a human analyst, and will allow better localization of the edges of the features in an image. Forming an image at a higher resolution than that of any of the low resolution images is possible if enough unique information is available; luckily, this is usually the case. Low resolution digital images are typically aliased (undersampled). If they are shifted with respect to one another with subpixel precision, more information is available than with a single image.

Quantitatively, an observation model is needed to relate the desired high resolution (HR) image to the observed low resolution (LR) images, or frames. This model is shown in Fig. 3. The LR frames are warped, blurred, and downsampled observations

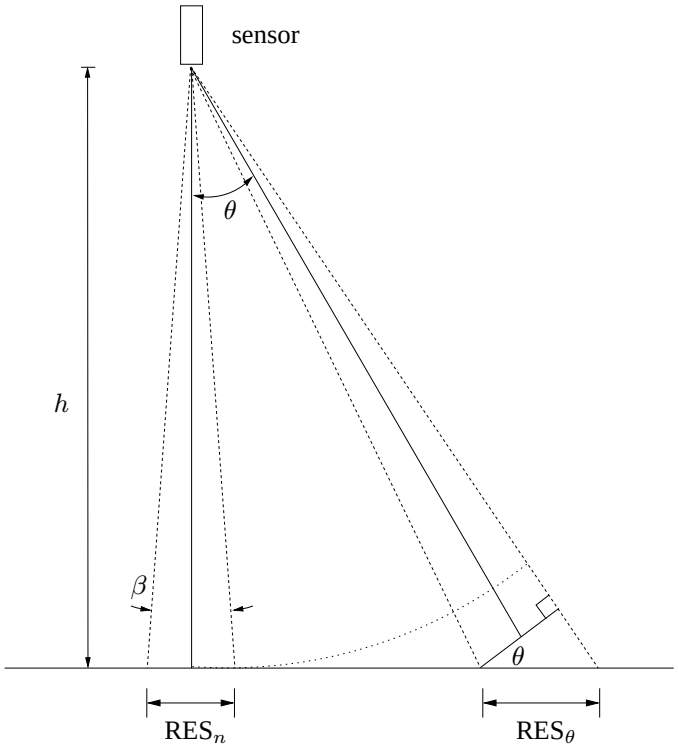

Fig. 2. Off-nadir vs. nadir resolution.

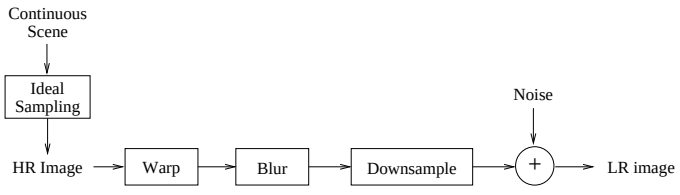

Fig. 3. Observation model relating low resolution (LR) images to a high resolution (HR) image.

of the HR image, and may have additive noise. Warping can involve translations, rotations, skew, or projective distortion from one LR frame to another. Blur may be caused by diffraction-limited optics, motion of the imaging system, motion of the viewed objects, or atmospheric turbulence. Sampling by a CCD array discretizes the locations of incoming photons.

Using the observation model above, the LR images may be input to a resolution enhancement algorithm [5] that tries to remove the degradations of the imaging process while using the unique information contained in each LR frame, resulting in an estimated HR image. The resulting HR estimate is discrete (sampled), but is not aliased, and is sampled to a finer grid than any of the sampling grids of the LR frames.

IV. Resolution Enhancement Algorithms

Resolution enhancement methods known as *super-resolution image reconstruction* algorithms are the starting point for the multi-angle resolution enhancement explored in this paper. Super-resolution is the extrapolation of the frequency content in an image, permitting the reconstruction of a digital image onto a grid with smaller pixels. Multi-frame super-resolution methods use several low-resolution input images to generate either a single high-resolution image or, in the case of video super-resolution, multiple high-resolution video frames. Reviews of approaches for super-resolution using multiple images are given in [3–5].

Super-resolution image reconstruction methods are divided into two approaches: frequency domain methods and spatial domain methods. Frequency domain methods are limited to global translational shifts between frames and spatially-invariant blurring. Consequently, they cannot be used for combining multi-angle remote sensing data, since the multi-angle frames may be rotated with respect to one another, may have perspective distortion, and may have irregular sample spacing. Spatial domain methods are much more flexible, allowing sophisticated imaging models to be used. One popular spatial domain method is set theoretic image resolution enhancement. Convex set theoretic methods for resolution enhancement have been around for several decades [16–24]. The most widely used algorithm of this type is the projection onto convex sets (POCS) algorithm [20, 21]. The POCS algorithm iteratively estimates a high resolution image from a set of low resolution images by performing simultaneous interpolation and restoration. Thus, POCS both increases the size of the image and removes the effects of blur due to the system PSF. The POCS method has many advantages for the resolution enhancement of images [20], including the flexible incorporation of prior knowledge, the ability to acquire the LR frames using any detector or scanning geometries including nonuniform sampling, the capability to compensate for different amounts and types of blur in each LR frame, and the ability to combine LR frames with different pixel sizes. The ability to input satellite images with different ground resolutions was an important factor for selecting POCS for the resolution enhancement.

The POCS algorithm uses prior knowledge about the imaging system to impose constraints on a high-resolution (HR) estimate of the original scene. The use of *a priori* knowledge helps the algorithm converge to a reasonable solution. Constraint sets may be formed for data consistency, energy bounds, amplitude bounds, spatial support bounds, etc. More precisely, each constraint defines a closed convex set C, which, for image reconstruction, is a set of images with a particular property. The object f is known *a priori* to belong to the intersection C_s of m closed convex sets C_1, C_2, ..., C_m,

$$C_s = \bigcap_{\alpha=1}^{m} C_\alpha, \tag{2}$$

where C_s is found by iteratively computing projections onto the convex sets (thus the name POCS):

$$f_{n+1} = P_m P_{m-1} \dots P_2 P_1 f_n. \tag{3}$$

The projection operator P_i maps the current estimate f to the closest point in the set C_i. Fig. 4 illustrates the POCS method, closely following a figure from Ref. [25]. One important constraint used in POCS ensures data consistency – that is, the HR estimate, when blurred and downsampled, must be consistent with the observed LR frames. This constraint is defined as

$$C_D = \{f : |r| \leq \delta\}, \tag{4}$$

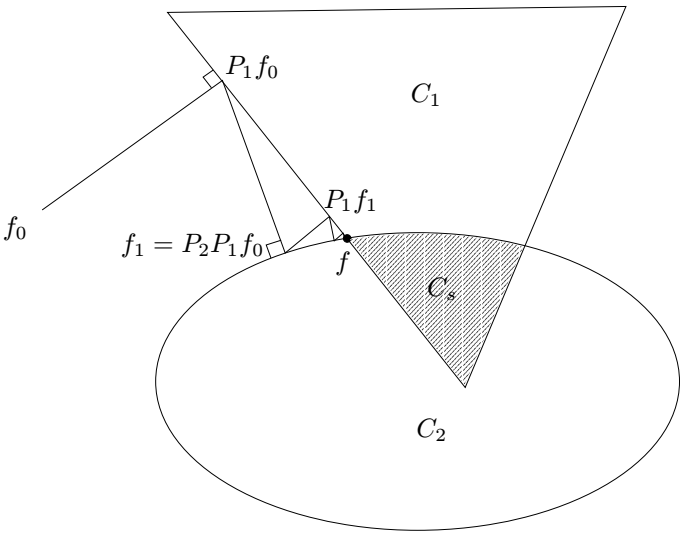

Fig. 4. The POCS algorithm for two constraint sets, shown converging to a solution f in the intersection set C_s.

where the residual r is the difference between a LR pixel value and a blurred region in the HR estimate

$$r(i,j) \doteq g(i,j) - \sum_k \sum_l f_n(k,l) h(i,j;k,l), \qquad (5)$$

and $\delta = c\sigma_v$, the confidence of the user in the observation for a noise standard deviation of σ_v, with the constant $c \geq 0$ found using a statistical confidence bound [21]. The projection of f onto the constraint set C_D is then

$$f_{n+1} = P_D f_n = \begin{cases} f_n + h\,(r-\delta)\,/\sum h^2 & \text{if} \quad r > \delta \\ f_n & \text{if} \quad -\delta < r < \delta \\ f_n + h\,(r+\delta)\,/\sum h^2 & \text{if} \quad r < -\delta \end{cases} . \qquad (6)$$

The POCS image reconstruction method using only the data consistency constraint may be summarized in the procedure shown in Figs. 5 and 6.

- Align (register) the LR images using known translation, rotation, and skew
- Until estimate f has converged:
  - For each pixel in each LR frame:
    - Find the non-integer location of the pixel center in the HR estimate
    - Apply blur to a neighborhood (window) of HR pixels corresponding to the estimated or known point spread function (PSF) of that LR frame
    - Subtract the average of the blurred region in the HR image from the LR pixel to find the residual r
    - Compute the new HR image values within the PSF window by adding the residual r multiplied by the PSF

Fig. 5. The POCS algorithm using the data consistency constraint.

V. Image Formation

Simulated off-nadir imagery is used in order to have control over the image registration and view angle parameters, as well as to provide sufficient data for analysis. To simulate imagery for input into our resolution enhancement algorithm, a model of the image formation process for multi-angle, remotely-sensed imagery is needed. The model must account for the optics of the imaging system, the changing view angle, and the sampling process of the detector array. We discuss each of these components in the following sections.

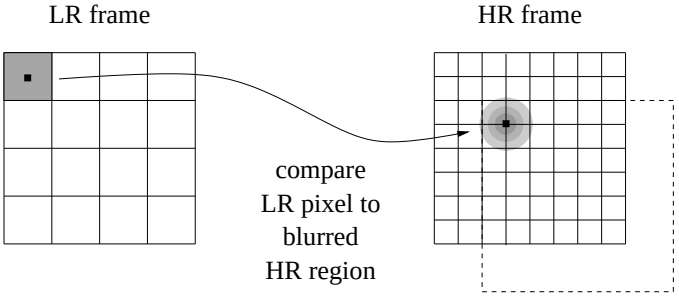

Fig. 6. Mapping the LR pixel to the HR estimate and computing the residual from the PSF applied to a local neighborhood.

A. Modeling the Optics

The optics are modeled using a linear, shift-invariant (LSI) imaging model, using the assumptions of quasi-monochromatic incoherent illumination, an aberration-free, diffraction-limited optical system, and imaging in the far-field [26, 27]. The system impulse response for an optical system is often called the point spread function (PSF). The intensity image, g, of an object f formed by an incoherent, LSI optical system with a PSF h may be illustrated as shown in Fig. 7. The imaging system

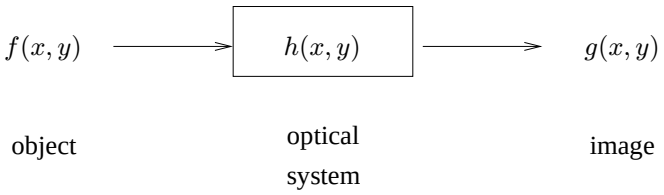

Fig. 7. Linear, shift-invariant imaging system model

is described equivalently as a two-dimensional spatial convolution of the object f with the PSF h,

$$g(x,y) = \int_{-\infty}^{\infty}\int_{-\infty}^{\infty} f(\xi,\eta) h(x-\xi, y-\eta) d\xi d\eta \qquad (7)$$

$$= (h * f)(x,y) \qquad (8)$$

where x, y are the coordinates in the image plane and ξ, η are the coordinates in the object plane.

It is useful to describe the optical system in terms of its frequency response, because the sharpness of edges and fine detail in a scene correspond to high frequencies in the Fourier domain. Taking the Fourier transform of Eq. 8, and after some rearranging of terms, we can express the incoherent optical system response in the frequency domain as

$$G(u,v) = H(u,v) F(u,v), \qquad (9)$$

where F is the Fourier transform of the object, G is the Fourier transform of the image, and $H(u,v)$ is the incoherent optical

transfer function (OTF) of the system [27, 28]. The OTF governs how spatial frequencies are preserved from the object to the image. Specifically, the incoherent OTF is defined as the normalized complex autocorrelation of either the aperture stop or the exit pupil, with a scaling factor [27]. For our purposes, it is sufficient to define an aperture function, $a(x, y)$, that could be a physically real pupil or a limiting aperture within the optical system. The blur due to the limiting aperture, and thus the OTF, fundamentally limits the resolution or amount of detail that may be seen in the image. The spatial frequency at which the OTF goes to zero is called the optical cutoff frequency, f_c. It is given by

$$f_c = \frac{D}{\lambda l} \tag{10}$$

where D is the aperture diameter, λ is the wavelength of the light, and l is the focal length of the optical system.

The aperture function used to generate blurred imagery is a simple circular pupil [26], $a(x, y)$, of radius r,

$$a(x, y) = \text{circ}\left(\frac{\sqrt{x^2 + y^2}}{r}\right). \tag{11}$$

The incoherent OTF, or complex autocorrelation of the aperture a, is given by

$$H_o(u, v) = \begin{cases} \frac{2}{\pi}\left[\cos^{-1}\left(\frac{f}{f_c}\right) - \frac{f}{f_c}\sqrt{1 - \left(\frac{f}{f_c}\right)^2}\right] & , f < f_c \\ 0 & , \text{otherwise} \end{cases} \tag{12}$$

where $f = \sqrt{u^2 + v^2}$ is the radial distance in the frequency plane [26]. To simulate diffraction-limited image blur due to the optical system, we first compute the two-dimensional Fourier transform of a high resolution "object" scene to obtain its spectrum. A standard FFT is used in the implementation. A circular aperture size is selected and the corresponding OTF is calculated. Next, the object spectrum is multiplied by the OTF, which removes the high frequencies present in the high-resolution image. The output of this step is a blurred image with the same number of pixels as the high resolution image. An example of an image blurred by diffraction effects by a circular aperture is shown in Fig. 8. For better visibility of the high frequencies, the object and image spectra are displayed using a logarithmic compression on the scaling.

To generate the multi-angled frames that would be viewed by a satellite-based sensor, two additional steps are required. First, the blurred image has a projective transform applied to it to simulate an off-nadir view angle. Then, the image is subsampled to model the detector array of the satellite system. These components of the system are presented next.

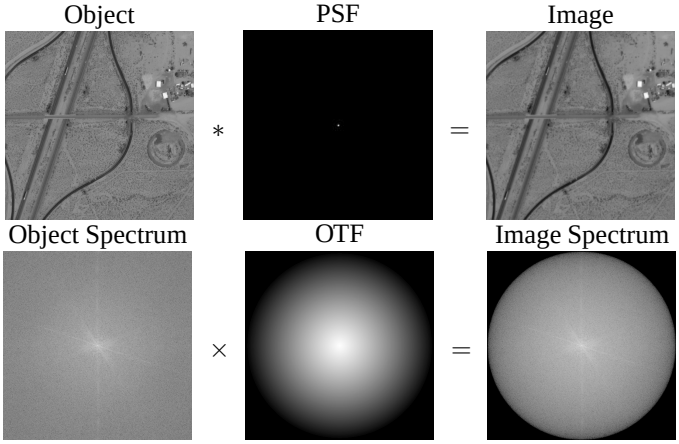

Fig. 8. High resolution object scene blurred by a circular aperture.

B. Modeling the Changing View Angle Between Frames

Between frames, we assume that the satellite carrying our imaging system has moved. Satellite motion can be very complex, but a simple model will be implemented to study the most important issue for multi-angle resolution enhancement problem: the view angle. Other issues, such as terrain, slope, elevation, and curvature of the Earth, are important, but are secondary to the issue of the increasing view angle from nadir and the subsequent increase in the pixel size due to the increased path length to the imaged scene as the angle increases.

It takes the MTI satellite 4.5 seconds to acquire a 12 km by 12 km image for all 16 spectral bands. The velocity of the satellite is 7 km/sec, thus the satellite travels approximately 31.5 km while acquiring a single image. The change in angle between the beginning of acquisition and the end of acquisition results in a change in the size of the projection of the detector line. The changing view angle (perspective) between nadir and the satellite with respect to the location of a feature on the ground may be modeled with a projective transform. The simplified geometry of an off-nadir image formed by a pushbroom sensor is shown in Fig. 9. The off-nadir field of view (FOV) in the cross-track direction, $\text{FOV}_{\text{O,C}}$, or swath width, is determined by the cross-track extent of the linear detector array projected onto the ground. Over $\Delta t = t_2 - t_1 = 4.5$ sec, the path length increases from l_1 to l_2, and the swath width becomes smaller. The off-nadir FOV in the along track direction, $\text{FOV}_{\text{O,a}}$, is determined by the image acquisition time and the off-nadir pointing angle at the midpoint of image acquisition θ_{ave}. Compared to the nadir along-track FOV, it is reduced by a factor of cosine squared (just as for the along-track off-nadir resolution shown previously in Fig. 2).

The homogeneous coordinate system is used to perform the required two-dimensional coordinate transforms [29]. An example of projective distortion due to a satellite viewing a scene from nadir and off-nadir is shown in Fig. 10. The off-nadir image appears scaled, but not much keystoning is visible because the distance from the sensor to the target (575 km for the MTI at nadir) is much larger than the extent of the image acquired (12 km by 12 km for the MTI).

C. Modeling the Detector Array Subsampling

The detector array effectively discretizes our image. This may be modeled by downsampling the blurred and transformed images to a grid with fewer pixels in each dimension. The subsampling process can introduce aliasing into the images. Recall from Sect. V-A that the optics of the system have an impulse response, or PSF_{optics}. If a point source is imaged by this system, it forms a diffraction pattern in the far field that consists

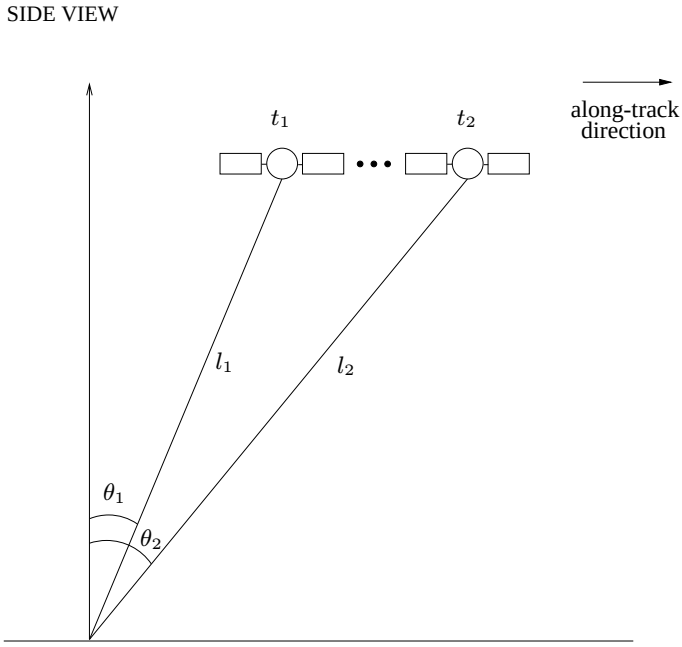

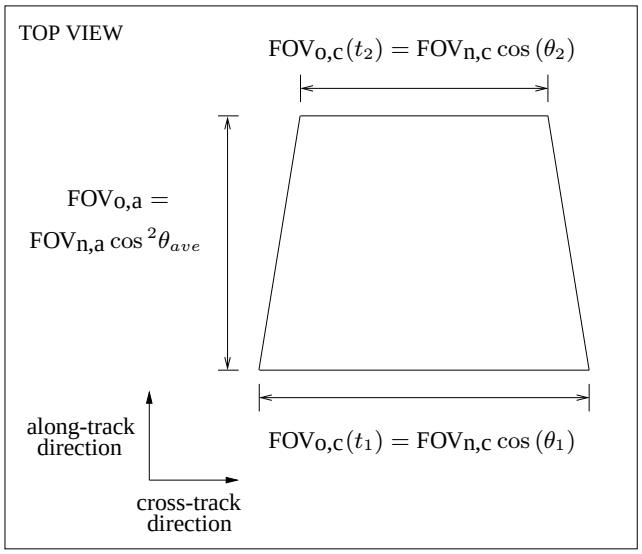

Fig. 9. Off-nadir geometry for a single band.

of bright concentric rings called the Airy pattern [26, 30]. The diameter of the central lobe is given by

$$d_{Airy} = 2.44\frac{\lambda f}{D}, \tag{13}$$

where λ is the wavelength of the point source, f is the focal length (the distance from the lens to the focal plane), and D is the diameter of the aperture or lens. The detectors located at the focal plane also have a PSF,

$$\text{PSF}_{detector}(x, y) = \text{rect}\left(\frac{x}{d_x}\right) \text{rect}\left(\frac{y}{d_y}\right) \tag{14}$$

where d_x and d_y are the sizes of a rectangular detector in the x and the y directions, respectively. For most detectors, the detector shape is square, or $d_{det} = d_x = d_y$. Assuming a 100% fill-factor for the detector array, when $d_{Airy} > d_{det}$, the system is called *optics-limited* [30]. When $d_{Airy} < d_{det}$, it is called *detector-limited*. These terms arise because the system PSF is given by the convolution of the optical and the detector PSF's,

$$\text{PSF}_{system} = \text{PSF}_{optics} * \text{PSF}_{detector}, \tag{15}$$

and the system OTF is given by the multiplication of the component OTF's,

$$\text{OTF}_{system} = \text{OTF}_{optics}\text{OTF}_{detector}. \tag{16}$$

The cutoff frequency of the optics OTF versus the detector OTF determines the whether aliasing is present. If high frequencies are allowed through the optics, but the detectors are not small enough, the high frequencies are aliased to low frequencies in the discretized output image.

It is important to understand the effects of aliasing when applying resolution enhancement algorithms to multispectral imagery because the degree of aliasing present varies with wavelength. For a system like the MTI, the same optics are used for both the visible and the IR bands, while the size of the detectors changes, resulting in more aliasing at the shorter wavelengths. For the MTI, $D = 36$cm and $f = 125$cm. In band A, $\lambda \approx 485$nm, so $d_{Airy} \approx 4.1\mu m$, much smaller than $d_{det} = 12.4\mu m$. The system is detector-limited in band A. In the IR bands, $\lambda \approx 10\mu m$, and $d_{Airy} \approx 84.7\mu m$, about twice the value of $d_{det} = 49.6\mu m$, meaning the IR bands for the MTI are optics-limited.

An example of an image after downsampling is shown in Fig. 11. Compared to the blurred image, the pixel size of the downsampled image is four times larger in each dimension, making high frequency detail much more difficult to see after sampling.

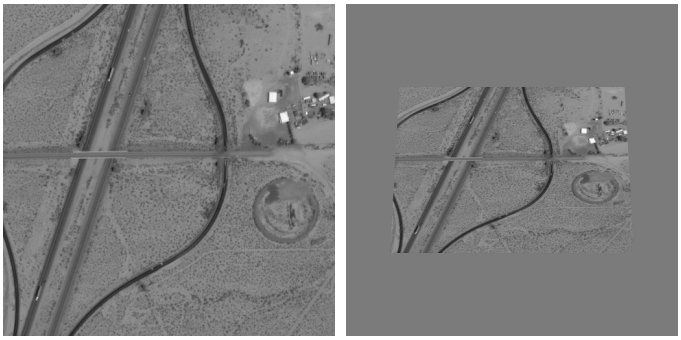

Fig. 10. Nadir and off-nadir image at 45° simulated using a projective transform with an orbital height of 575 km.

VI. The Elliptical Gaussian System PSF Model

The POCS algorithm requires knowledge of the system PSF. With the added complication of off-nadir frames, the known or estimated PSF must be warped; the projective transform model requires a mapping of the system PSF from every pixel in each LR frame to the HR estimate, resulting in a distorted PSF in the HR grid. The computation of the projected system PSF can be time consuming [4]. However, it is possible to use an approximate mapping of the PSF using an affine transform rather

Fig. 11. Blurred image vs. blurred, 4X downsampled image

than a projective transform and keep the processing time reasonable. For off-nadir images simulated using the parameters of the MTI sensor, the primary transformation of the off-nadir image is a change in scale; the perspective keystoning is small due to the very large distance from the satellite to the ground. Therefore, the affine transform is reasonable for mapping the PSF of a satellite sensor from the off-nadir LR frames to the HR estimate grid. Using the affine mapping, the projected PSF will be the same for every pixel in a given LR frame, thus reducing the computational time considerably.

First, a model for the system PSF in a nadir viewing case must be selected. Two-dimensional Gaussian functions, both circular and elliptical, have been used previously to model the system PSF of a satellite [31–33]. Likewise, a 2D Gaussian function is used to approximate the system PSF in this paper. The Gaussian PSF is circularly symmetric at nadir, assuming the optics do not have distortions. Mapping the PSF from a given off-nadir LR frame to the HR estimate grid with an affine transform results in an elliptical Gaussian PSF, given by

$$\text{PSF}(x,y) = \frac{1}{2\pi\sigma_x\sigma_y} e^{-x^2/2\sigma_x^2} e^{-y^2/2\sigma_y^2} \qquad (17)$$

where σ_x and σ_y are determined by scaling the circularly symmetric nadir PSF of width σ by a cosine or a cosine-squared factor of the off-nadir look angle θ, so that

$$\sigma_x = \frac{\sigma}{\cos\theta} \quad \text{and} \quad \sigma_y = \frac{\sigma}{\cos^2\theta} \qquad (18)$$

in the cross-track and in the along-track directions, respectively. The PSF is normalized so that the area under the PSF is constant to ensure that the weighting during the blur step of the POCS algorithm is correct.

VII. Validation of POCS using multi-look imagery

To measure the performance of the resolution enhancement algorithm, a quantitative image quality metric is needed. The SNR improvement, or ISNR (measured in dB), is a useful metric for image restoration [34] and will be used here. It is given by

$$\text{ISNR}(f,\tilde{f},g) = 10\ \log_{10}\left(\frac{\sum[f-g]^2}{\sum\left[f-\tilde{f}\right]^2}\right). \qquad (19)$$

It measures the distance between the original scene f and a restored image $\tilde{f}$ as well as the distance between the original scene f and the degraded image g. This metric assumes that the original, degraded, and restored images are the same size. Since the degraded images here are the LR frames, which are at a lower resolution than that of the original and HR estimate, some modification to the ISNR metric must be made in order use it to measure resolution enhancement performance. A baseline "degraded" image g may be formed by interpolating (i.e., bilinear interpolation) the nadir LR frame to the same size as the original image and the HR estimate. Then, the ISNR will provide a measure of how much better the restored image is compared to the interpolation of just one LR frame, or roughly, how much additional information has been gained from the off-nadir frames. Obviously, when real imagery is used rather than simulated imagery, the ISNR cannot be computed since the "original" image f is not known.

A. Combining Two-look Imagery

The performance of the POCS algorithm with simulated two-look imagery is examined in this section. Using the multi-angle image simulation tools developed in the previous section, test data consisting of a nadir image and one off-nadir image are formed. The test input used is an image acquired by the MTI instrument over Albuquerque, NM, over the Isotopes Park baseball field. The image is a 128×128 crop from band A (the visible "blue" band), and is shown in Fig. 12. This image allows a quantitative measure of the image improvement possible for remotely-sensed imagery at visible wavelengths, specifically for the MTI sensor.

Fig. 12. The original "Isotopes" MTI image, sized 128×128 pixels.

The POCS algorithm is applied to two images, one at nadir and one at an off-nadir angle θ, to observe the effect of the off-nadir view angle on convergence. The basic parameters of the MTI instrument are used to model the off-nadir image geometry. The height of the sensor is assumed to be 575 km, and

the field-of-view (FOV) is approximately that of the MTI instrument. Unlike the MTI, the sensor is modeled by a circular aperture in front of a 64×64 pixel 2D CCD array. The HR grid is defined to be 128×128 pixels, meaning that the output resolution will be twice that of the input images in both the x and y directions (four times the number of pixels). However, this sampling grid is finer than the "true" resolution expected, since two images with optimum shifts and no angular movement allows a theoretical resolution increase of only 1.4 from simple geometry.

The modeled input LR frames are shown in Fig. 13, with the nadir LR frame shown larger in Fig. 14 for comparison with the original image in Fig. 12. A simple bilinear interpolation of the nadir image is shown in Fig. 15. The ISNR curves for the two-image case are shown in Fig. 16, and a representative HR image is shown in Fig. 17. A visual inspection shows that the POCS restored image contains more edge detail than the bilinearly-interpolated frame. Details such as the divided road lanes and parking lot rows are more apparent in the restored HR estimates, with details again varying depending on which off-nadir angle was used. The best two-angle combination for this data occurs at $\theta = 0^\circ, 10^\circ$, with an ISNR of 5.4 dB.

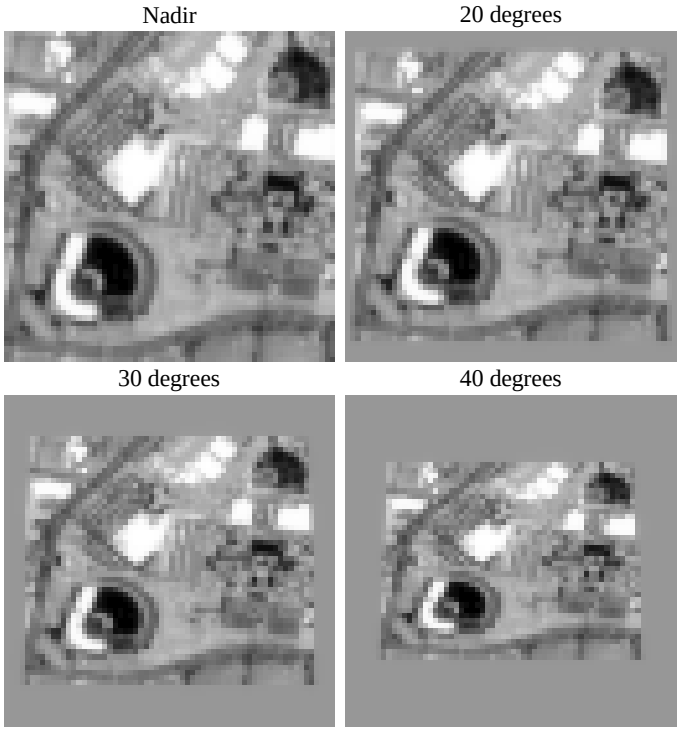

Fig. 13. The simulated multi-angle LR "Isotopes" frames used as input to the POCS algorithm, 64×64 pixels.

B. Combining Multi-look Imagery

The two-look case showed modest visual improvement in the spatial resolution and an ISNR improvement between 4.1 dB and 5.4 dB; to determine how many images are needed, and at what angles, for better results, the performance of the POCS algorithm with simulated multi-look imagery is examined. Ten images, one nadir and nine off-nadir, are combined to form a

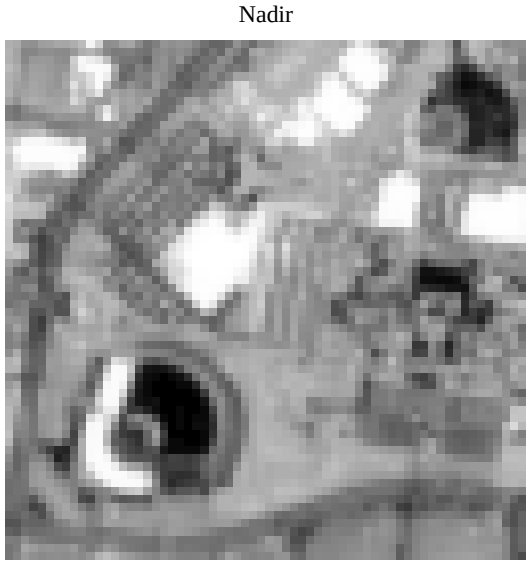

Fig. 14. Closeup of nadir LR "Isotopes" frame, 64×64 pixels.

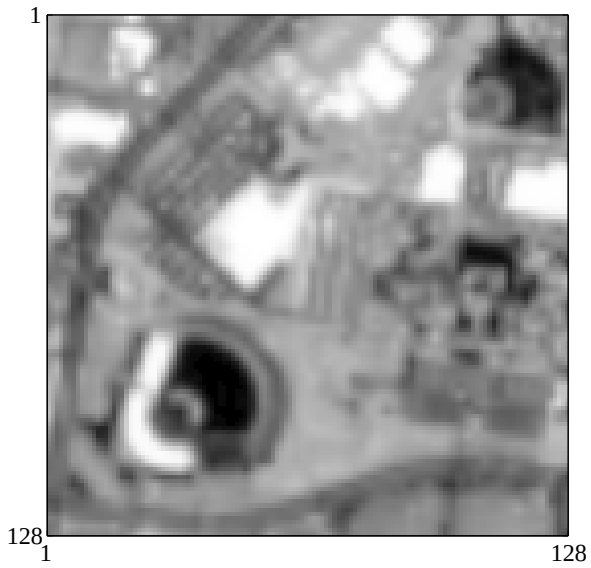

Fig. 15. Bilinear interpolation of nadir LR "Isotopes" frame.

HR image. The parameters used to model the image geometry are the same as those for the MTI instrument.

The effect of increasing the off-nadir angle on the ISNR is shown in Fig. 18. The highest ISNR occurs at 40°, using six LR frames, after 8 epochs. The inclusion of the image at 48° makes the peak ISNR lower and causes divergence of the POCS solution; at this angle, the off-nadir resolution is more than twice that of the nadir resolution. Since the MTI acquires its second look near 50° or 55°, it is therefore unlikely that the standard off-nadir data could be used successfully for resolution enhancement; tasking of the satellite at smaller look-angles is needed for this application.

The number of images needed when restoring to a grid at twice the resolution of the LR frames is examined next. Ten images with 5° separation are generated, with a maximum angle of 45° (designed to be less than 48° since the images fail

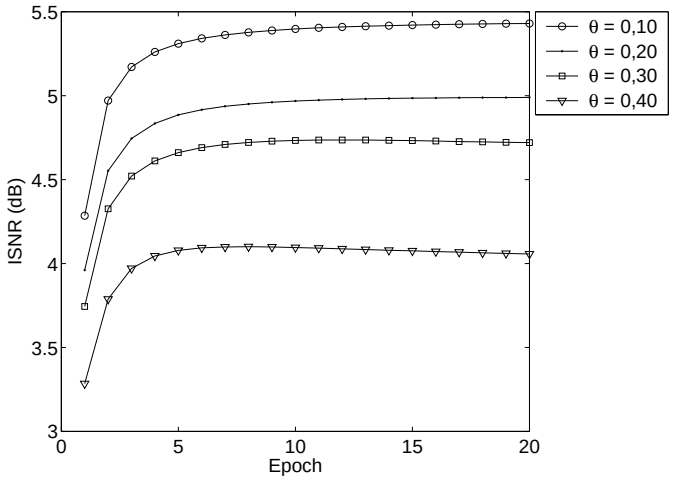

Fig. 16. Improvement in SNR for the "Isotopes" image using two frames, one nadir and one off-nadir at various look angles θ.

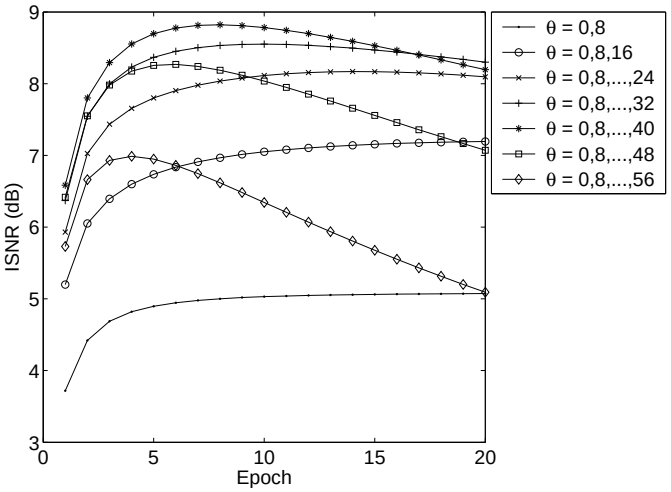

Fig. 18. Improvement in SNR using multiple frames at increasing angles.

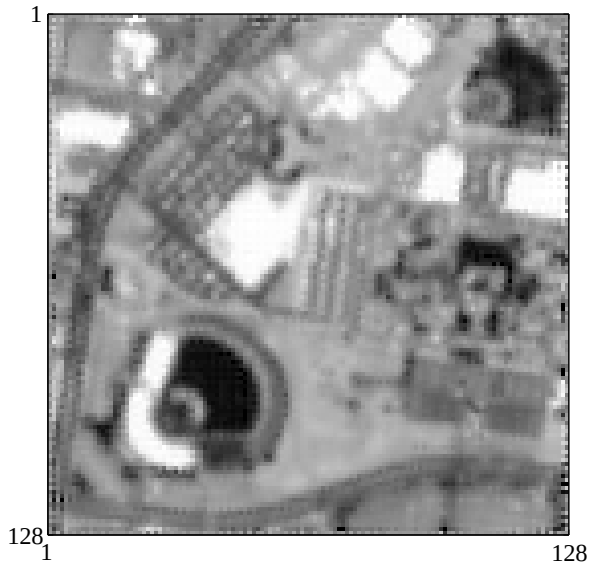

Fig. 17. The HR estimate using two frames, one nadir and one off-nadir at $\theta = 30^\circ$.

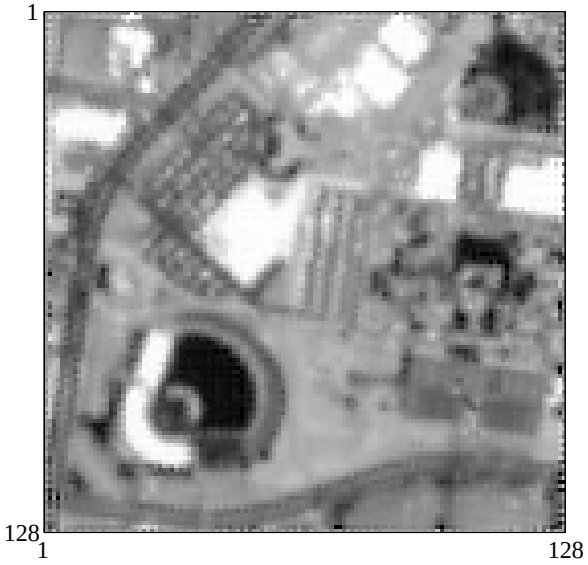

Fig. 19. The HR estimate using six frames, $\theta = 0^\circ, 8^\circ, 16^\circ, 24^\circ, 32^\circ, 40^\circ$.

to provide helpful information past that point). Fig. 20 shows the ISNR curves with $\Delta\theta = 5^\circ$ up to a maximum off-nadir angle of $\theta = 45^\circ$. The maximum ISNR is close to 9 dB. After combining five or six images, the ISNR is not made better by combining more images, but the ISNR values do not get worse, either. Therefore, six LR frames are ideal for this viewing scenario, as long as the images are acquired for $\theta < 48^\circ$ off-nadir so that they do not cause divergence of the POCS algorithm.

C. Combining Symmetric Three-look Imagery

The two-look experiments of Sect. VII-A assumed that the imaging system operated like the MTI sensor, first acquiring a nadir image and then pointing back to acquire a second image. A logical improvement in the image collection is to begin taking images as soon as the ground target is within view at some forward-pointing off-nadir angle, and then continue to point the satellite and take imagery until the sensor has passed over the ground target and is pointing backward at some maximum off-nadir angle. This approach allows more images at look angles close to nadir to be collected. Since near-nadir imagery has the highest resolution (the IFOV is smallest when the distance from the satellite to the ground is at a minimum), as many images as possible should be taken close to nadir. The number of images that may be taken is limited by the time required to re-point the satellite. At a minimum, three images, one at nadir and two at symmetric off-nadir positions $\pm\theta$, should be used to maximize the quality of the data input to a resolution enhancement algorithm. To explore the idea of using symmetric off-nadir images, the POCS algorithm is applied to simulated three-look imagery. The LR dataset is formed from a nadir image ($\theta = 0$), a forward-pointing off-nadir image at $-\theta$, and a backward-pointing off-nadir image at $+\theta$. As a representative example, the $\Delta\theta = 20^\circ$ case for symmetric viewing gives an ISNR of 6.2 dB, while the asymmetric case gives an ISNR of 6.9 dB, an improvement of 0.7 dB. The ISNR curves are shown

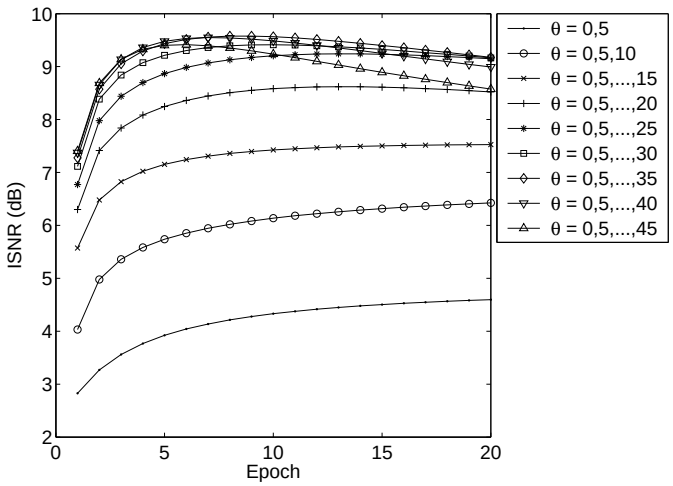

Fig. 20. The ISNR for 2 to 10 frames, $\theta = 0°, 5°, 10°, ..., 45°$.

in Fig. 21. As discussed further by the authors in Ref. [35], symmetric viewing with $\theta = -15°, 0°, 15°$ gives a 7.5 dB improvement compared to a similar 7.7 dB improvement using $\theta = 0°, 13.3°, 26.7°, 40°$; three symmetric frames are needed compared to four asymmetric frames for equivalent improvement of the "Isotopes" image. Therefore, symmetric viewing is better than asymmetric viewing for POCS resolution enhancement. It may be surmised that symmetric viewing gives a better ISNR than the asymmetric viewing case since the imaging angles are closer to nadir.

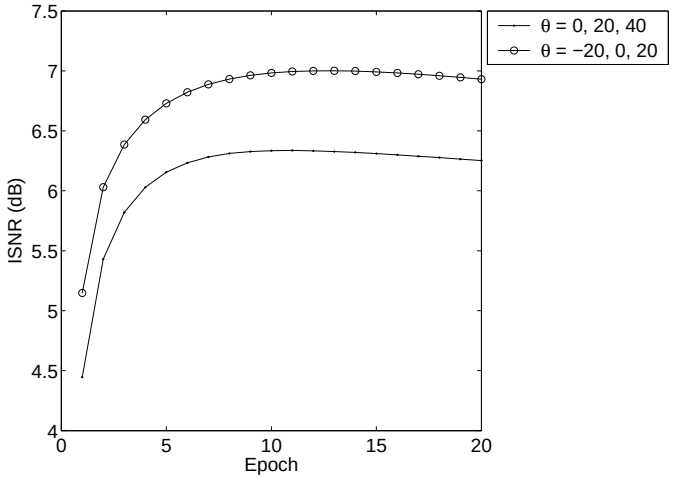

Fig. 21. Improvement in SNR for the "Isotopes" MTI image using three frames, one nadir and two off-nadir at look angles $\pm\theta$.

VIII. Misregistration Effects

The cases considered thus far have been ideally registered. In practice, perfect registration of satellite images is not possible. To put the previous error analysis in context, the effect of misregistration on ISNR is considered. Using symmetric three-look imagery at -15°, 0°, 15°, a uniform subpixel misregistration of the nadir LR image is modeled. The misregistration is in units of a fraction of a pixel in the along-track direction. The ISNR curves are shown in Fig. 22. As the misregistration Δx increases, the peak ISNR decreases as expected. The POCS algorithm converges well for $\Delta x < 0.1$ pixel. For larger misregistration, resolution enhancement still occurs as measured by ISNR, but artifacts are seen in the HR image. For a misregistration of $\Delta x = 0.1$ pixels for the symmetric three-look case, the ISNR is 1.25 dB less than that of the perfect registration, while $\Delta x = 0.2$ pixels decreases the peak ISNR by about 2.2 dB. The result of combining three-look imagery with a 0.2 pixel misregistered nadir frame is shown in Fig. 23. Despite the jagged artifacts due to misregistration, the image appears visually improved compared to the nadir LR frame. Prior studies have shown that a registration of $\Delta x < 0.2$ pixel is needed to do change detection using satellite imagery [36, 37]. In addition, a rule of thumb is given in Ref. [24], stating that for optimal resolution enhancement of K LR images, a (1/K)-pixel or smaller rms registration error is needed. The results here are consistent with these earlier studies.

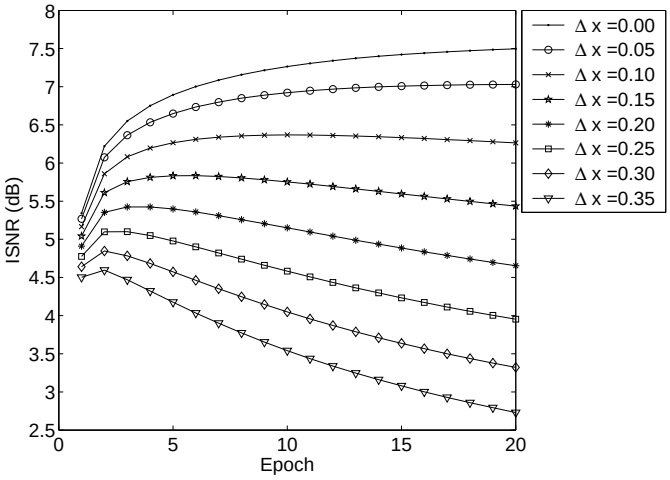

Fig. 22. Improvement in SNR for the "Isotopes" MTI image using three frames at $-15°, 0°, +15°$, with the nadir image misregistered by Δx pixels.

IX. Noise Effects

The effect of image observation noise on POCS enhancement is examined in Refs. [21]and [22]; there, the authors modified the POCS algorithm of Ref. [20]to account for observation noise. We briefly examine the effect of observation noise on the enhancement of three-look imagery. Additive white Gaussian noise is applied to each of the three LR frames independently to form noisy images at the 10, 20, 30 and 40 dB SNR level. The POCS confidence bound δ of Eq. 4 first is set to zero to ignore observation noise, then is set to $\delta = c\sigma_v$, where σ_v is set to the noise standard deviation, and $c = 1$, to show how the modified POCS algorithm of Ref. [21] reduces noise amplification. The INSR curves for the enhanced noisy images are shown in Figs. 24 and 25. For high SNR's (30 dB or higher), setting $\delta = 0$ is best. As discussed in Ref. [22], small δ values give sharp images at the expense of added noise, like an inverse filter. For low SNR's, increasing δ helps prevent a noisy solution, as shown by the improved ISNR's for the 10 and 20

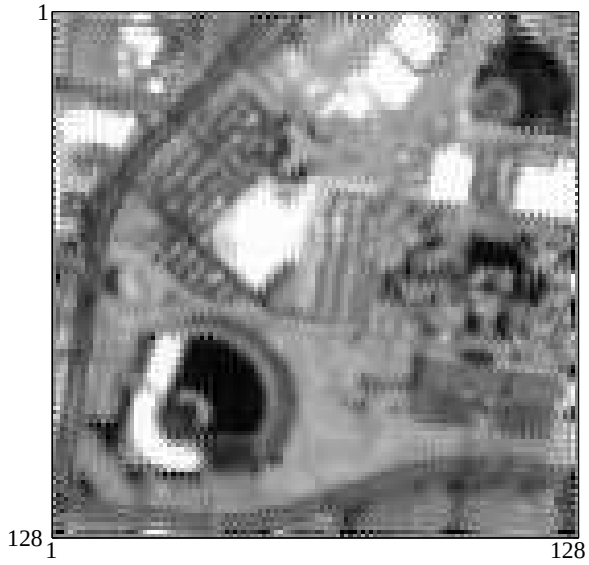

Fig. 23. The HR estimate using three frames at $-15^\circ, 0^\circ, +15^\circ$ and $\Delta x = 0.2$ pixel.

dB three-look images. However, the POCS algorithm did not improve the SNR of the 10 dB image sets. Therefore, it may be concluded that it is important to have SNR's above 20 dB to improve multi-look imagery.

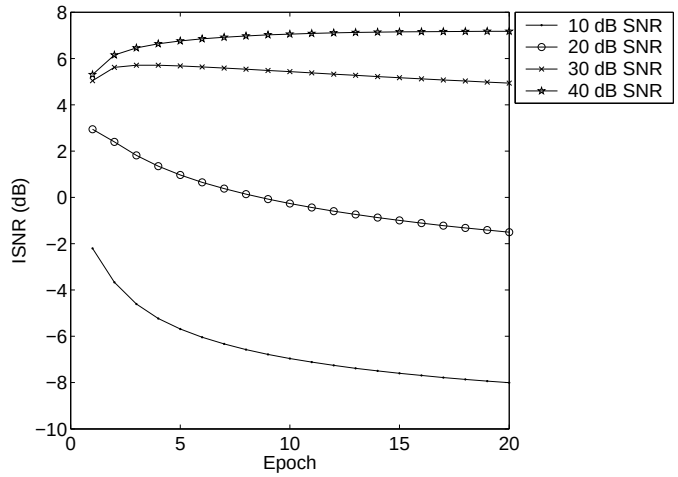

Fig. 24. Improvement in SNR for the "Isotopes" MTI image using three frames at $-15^\circ, 0^\circ, +15^\circ$, with noise, $\delta = 0$.

X. Atmospheric and BRDF Effects

Several pre-processing steps can improve the results of resolution enhancement algorithms when applied to multi-angle, remotely-sensed images. The pre-processing issues considered here include atmospheric correction and directional reflectance properties of materials. The effects of the atmosphere ideally should be removed from the multi-angle satellite images before fusing them because the path length from the sensor to the surface of the earth becomes larger with increasing angles with respect to nadir, and the sun's position is different from one image to another. For small angles and short times between subsequent images, atmospheric effects may not change dramatically and could be neglected. However, removing the atmospheric effects allows a retrieval of ground reflectance, which is needed for another pre-processing step: bidirectional reflectance distribution function correction.

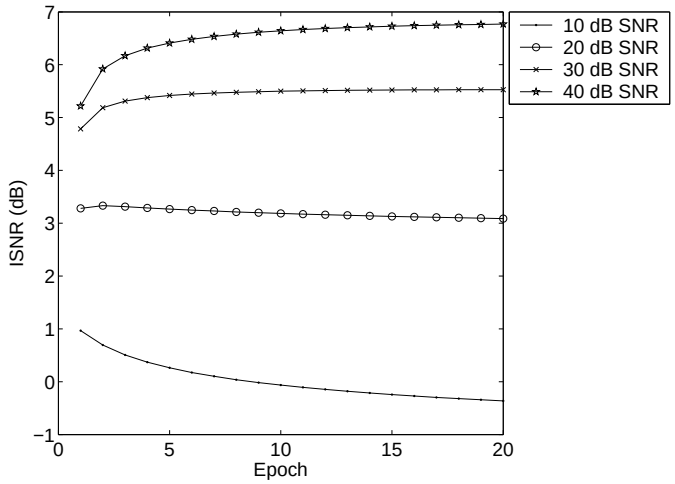

Fig. 25. Improvement in SNR for the "Isotopes" MTI image using three frames at $-15^\circ, 0^\circ, +15^\circ$, with noise, $\delta = c\sigma_v$, $c = 1$.

In this section, the "Isotopes" MTI image is used to generate multi-angle datasets with BRDF or atmospheric effects. The upwelled radiance, also called the path radiance, is modeled to determine how it affects the resolution enhancement of multi-angle imagery. In a separate simulation, the grass lawn of the baseball field in the "Isotopes" image is altered to simulate the effect of BRDF with changing view angle. A radiative transfer code is normally used to model path radiance. However, with some reasonable assumptions, a very simple model of atmospheric path radiance may be formed. Assuming a sensor view angle of no greater than 60° and a thin atmosphere, the optical depth as a function of the angle may be considered to be directly proportional to the increase in path length ([38], p. 105):

$$\delta(\theta) \propto \sec\theta. \tag{20}$$

An estimate of the path radiance at nadir, $L_p(0)$, may be found by measuring the pixel value in an area of dark vegetation, such as the baseball field in the "Isotopes" image. An off-nadir image at view angle θ with atmospheric path radiance effects is then simulated by adding a constant off-nadir path radiance value, $L_p(\theta)$, to all pixels in the original image prior to applying the projective transform and downsampling steps:

$$L_p(\theta) = L_p(0) * (\sec\theta - 1.0). \tag{21}$$

The "Isotopes" image with modeled path radiance is shown in Fig. 26, using look angles of $\theta = -50^\circ, 0^\circ, +50^\circ$. The off-nadir images are brighter due to the increased upwelled radiance at the longer off-nadir path length. If the POCS algorithm is applied to the uncorrected data set, the algorithm diverges, as shown in Fig. 27, resulting in an unacceptable "speckled" HR estimate. Uncorrected three-look data sets are formed for various off-nadir angles to determine at what angle the POCS

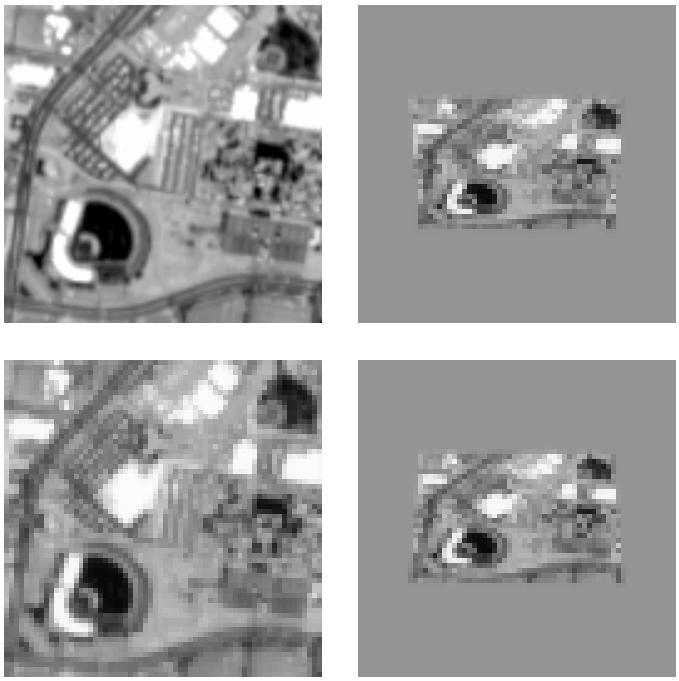

Fig. 26. The original "Isotopes" MTI image (upper left) and the three-look images with modeled atmospheric path radiance (upper right at -50°, lower left at 0°, and lower right at $+50^\circ$).

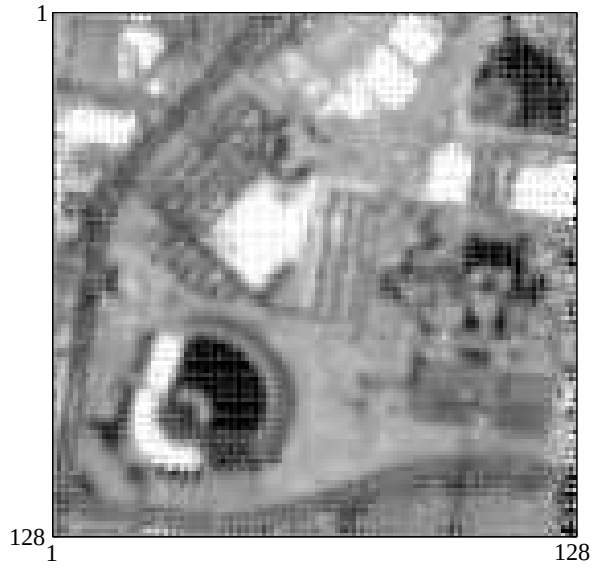

Fig. 27. The HR estimate for $\theta = -50^\circ, 0^\circ, +50^\circ$ without atmospheric correction. The different contrast in the LR frames prevents POCS from giving good results. The ISNR is 2.07 dB.

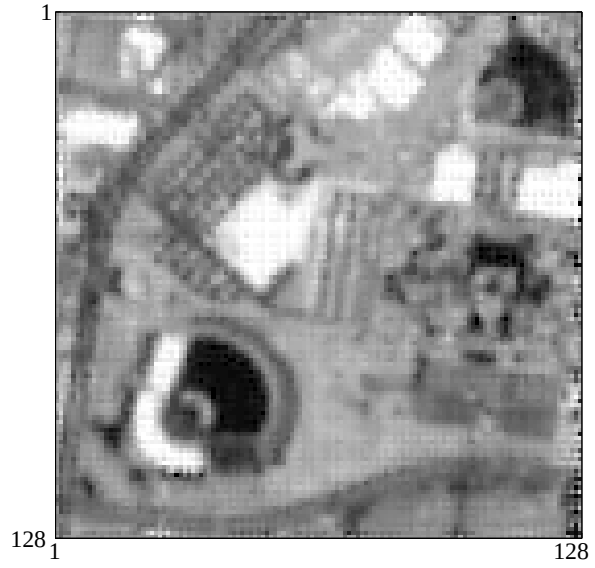

Fig. 28. The HR estimate with the bias subtracted from the LR frames to compensate for off-nadir atmospheric path radiance. The pixels in the baseball field no longer look speckle; some artifacts remain due to the large off-nadir imagery at $\pm 50^\circ$. The ISNR is 2.79 dB here, an improvement of 0.72 dB over the uncorrected case.

algorithm diverges if given data that has not had atmospheric correction applied. Compared to the ISNR values for three-look imagery without modeling path radiance, the ISNR values are approximately 1.1 dB lower. Imagery at $\theta > 40^\circ$ begins to pose a problem for POCS for this dataset. After a few iterations, the inconsistent LR data causes ringing in the HR estimate. It may be concluded that atmospheric correction is needed when the LR frames are acquired at $\theta > 40^\circ$ to ensure convergence of the algorithm under thin atmosphere conditions. For larger optical depths, atmospheric correction is required for even smaller off-nadir angles. Assuming the off-nadir path radiance is constant over the image, it is straightforward to pre-correct the imagery by subtracting the bias due to atmospheric path radiance even if the off-nadir angles are not known. Alternatively, the contrast of the LR frames could be matched using histogram equalization. The HR estimate with the atmospheric term subtracted for the $\theta = -50^\circ, 0^\circ, +50^\circ$ three-look imagery is shown in Fig. 28. The final ISNR is 2.79 dB with the correction. For comparison, without correcting the atmospheric path radiance, the ISNR is 2.07 dB. Thus, the bias subtraction improves the HR estimate by 0.72 dB. The simple bias removal is therefore an effective method to ensure that the LR frames are "consistent," as long as one can assume that the atmospheric path radiance is constant over the entire image, and if the enhanced HR image is going to be used for visual interpretation rather than to derive secondary remote sensing products. The best correction when physical units are needed is to model the atmosphere with a radiative transfer code.

Next, the effects of directional reflectance are examined. The test image contains a baseball field that is composed of grass turf. To simulate the effect of BRDF on the resolution enhancement, the pixels composing the field are scaled to simulate the change in radiance expected at off-nadir angles. The simulated BRDF-scaled images are input to the POCS algorithm and the ISNR is computed. The BRDF scaling used is taken from a study by Sandmeier, et al. [39] that measured the reflectance of a grass lawn in the laboratory using a transportable field goniometer (FIGOS). The data were provided in a graph of bidirectional reflectance factor (BRF) versus view zenith angle; for this experiment, the values were measured from the graph and stored in a lookup table of BRF vs. angle, so the values are approximate. The BRF R is the ratio of the reflected energy from a material of interest to the energy that is reflected from an ideal

Lambertian surface. A Lambertian surface is one that reflects energy equally in all directions, or

$$L_{reflected} = \frac{\rho E_{incident}}{\pi}, \tag{22}$$

where L is radiance in Watts/m^2/sr, E is the incident irradiance from the sun, and ρ is the reflectance. The BRF is given by

$$R = \pi f_r = \frac{\Phi_{sample}}{\Phi_{lambertian}}. \tag{23}$$

To scale the grass baseball field pixels to model BRDF effects, the BRF at the view angle of an off-nadir image is found in the lookup table, then the BRF at nadir is found. The ratio of the BRFs provides the scale factor for the grass pixels:

$$\Phi_{sample}(\theta_o) = \frac{R(\theta_o)}{R(\theta_n)} \Phi_{sample}(\theta_n). \tag{24}$$

The ISNR curves for the three-look imagery with uncorrected BRDF effects are shown in Fig. 29. For $\theta > 20^\circ$, the POCS algorithm starts to diverge. Note that BRDF results will vary depending on the type and amount of non-Lambertian material. However, these results indicate that if highly non-Lambertian materials are in the scene that is to be resolution-enhanced, then BRDF correction may be necessary.

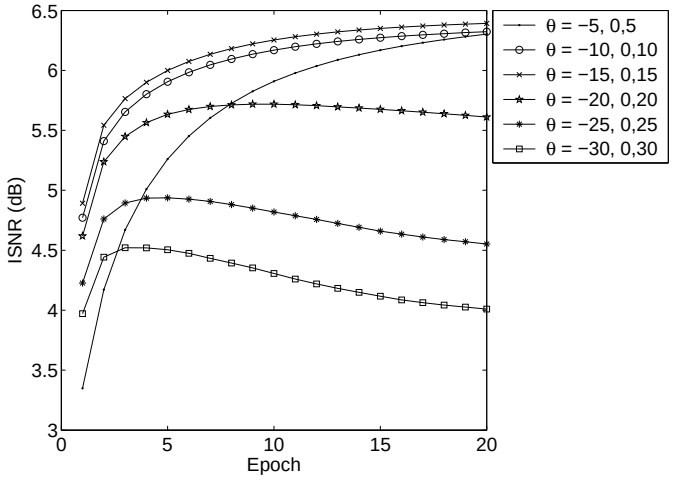

Fig. 29. The ISNR for three-look imagery with uncorrected BRDF effects, using different off-nadir angles.

XI. Conclusions

To do resolution enhancement, the sensor should be configured to acquire imagery at symmetric view angles in order to collect as many images as possible, as close to nadir as possible, within as short a time as possible. Practical constraints on the number of images that may be acquired during one overpass limit the resolution improvement that is possible for remotely-sensed imagery. Images acquired too far off-nadir can lead to divergence of the POCS algorithm. For the simulated images here, using views farther than 48° off-nadir were counterproductive for this reason. From the simulations here, three symmetric LR frames can improve the imagery by 7.5 dB when restored on a grid twice the size of the LR frames. Seven images can provide an improvement in SNR of 9.5 dB. Using more than seven asymmetric frames did not improve the ISNR results. Misregistration and observation noise both reduce the effectiveness of the POCS resolution enhancement algorithm. For the data here, a misregistration of 0.2 pixels gave a peak ISNR of 5.4 dB, 2.2 dB lower than the perfectly registered case. However, edge details such as divided roadways are still visible after enhancing the misregistered imagery. Therefore a misregistration up to 0.2 pixels appears to be acceptable for combining three-look images. For the simulations here, noisy three-look imagery with a 20 dB or greater SNR were enhanced by an ISNR of 5 dB or greater. Atmospheric and BRDF effects also should be considered when combining multi-angle images. Atmospheric correction is needed when $\theta > 40^\circ$, and directional reflectance prevents convergence of POCS when $\theta > 20^\circ$. These results indicate that the LR frames should be acquired at small angles, or $\theta \leq 20^\circ$. The MTI instrument as currently configured acquires two images 55 degrees apart; currently, we do not have multi-angle single-pass imagery that could be combined using the POCS method described here. Nonetheless, the technique of combining multi-angle imagery to enhance spatial resolution is promising for future pointable, multi-look imaging systems like MTI, if care is taken to design the satellite for fast, multiple image acquisition and accurate spatial registration.

References

[1] M. Cook, B. Peterson, G. Dial, L. Gibson, F. Gerlach, K. Hutchins, R. Kudola, and H. Bowen, "IKONOS technical performance assessment," in *Proc. SPIE*, vol. 4381, 2001, pp. 94–108.

[2] T. Miers and R. Munro, "Ball global imaging system for earth remote sensing," in *Proc. SPIE*, vol. 4169, 2001, pp. 362–373.

[3] S. Borman and R. L. Stevenson, "Super-resolution from image sequences-a review," in *IEEE Midwest Symposium on Circuits and Systems*, Aug. 1998, pp. 374–378.

[4] ——, "Image resampling and constraint formulation for multi-frame super-resolution restoration," *Proc. SPIE*, vol. 5016, no. 1, pp. 208–219, Jan. 2003.

[5] S. C. Park, M. K. Park, and M. G. Kang, "Super-resolution image reconstruction: a technical overview," *IEEE Signal Processing Mag.*, pp. 21–36, May 2003.

[6] T. M. Lillesand and R. W. Kiefer, *Remote sensing and image interpretation*. John Wiley & Sons, 2000.

[7] J. J. Szymanski, W. Atkins, L. Balick, C. C. Borel, W. B. Clodius, W. Christensen, A. B. Davis, J. C. Echohawk, A. Galbraith, K. Hirsch, J. B. Krone, C. Little, P. Maclachlan, A. Morrison, K. Pollock, P. Pope, C. Novak, K. Ramsey, E. Riddle, C. Rhode, D. Roussel-Dupré, B. W. Smith, K. Smith, K. Starkovich, J. Theiler, and P. G. Weber, "MTI science, data products and ground data processing overview," *Proc. SPIE*, vol. 4381, pp. 195–203, 2001.

[8] P. G. Weber, B. C. Brock, A. J. Garrett, B. W. Smith, C. C. Borel, W. B. Clodius, S. C. Bender, R. R. Kay, and M. L. Decker, "Multispectral Thermal Imager mission overview," *Proc. SPIE*, vol. 3750, pp. 340–346, 1999.

[9] D. Diner, J. Beckert, T. Reilly, C. Bruegge, J. Conel, R. Kahn, J. Martonchik, T. Ackerman, R. Davies, S. Gerstl, H. Gordon, J.-P. Muller, R. Myneni, P. Sellers, B. Pinty, and M. Verstraete, "Multi-angle imaging spectroradiometer (MISR) instrument description and experiment overview," *IEEE Trans. Geosci. Remote Sensing*, vol. 36, no. 4, pp. 1072–87, July 1998.

[10] M. C. Edwards, D. Llewellyn-Jones, and H. Tait, "The Advanced Along Track Scanning Radiometer: validation and early data," *IEEE International Geoscience and Remote Sensing Symposium*, pp. 614–616, June 2002.

[11] J. Bermyn, "PROBA – PRoject for On-Board Autonomy," *Air & Space Europe*, vol. 2, no. 1, pp. 70–76, Jan./Feb. 2000.

[12] European space agency. Proba: Facts and figures. [Online]. Available: http://www.esa.int/export/esaMI/Proba_web_site/ESA6AKTHN6D_0.html

[13] J. Theiler, A. Galbraith, P. Pope, K. Ramsey, and J. Szymanski, "Automated coregistration of MTI spectral bands," *Proc. SPIE*, vol. 4725, pp. 314–327, 2002.

[14] R. Kay, S. Bender, T. Henson, D. Byrd, J. Rienstra, M. Decker, N. Rackley, R. Akau, P. Claassen, and R. K. et. al., "Multispectral Thermal Imager (MTI) payload overview," *Proc. SPIE*, vol. 3753, pp. 347–358, July 1999.

[15] J. A. Richards, *Remote Sensing Digital Image Analysis*. Springer-Verlag, 1993, p. 51.

[16] A. Lent and H. Tuy, "An iterative method for the extrapolation of bandlimited functions," *Journal of Mathematical Analysis and Applications*, vol. 83, pp. 554–565, 1981.

[17] D. C. Youla and H. Webb, "Image restoration by the method of convex projections: Part 1 - theory," *IEEE Trans. Med. Imag.*, vol. MI-1, no. 2, pp. 81–94, Oct. 1982.

[18] M. I. Sezan and H. Stark, "Image restoration by the method of convex projections: Part2 - applications and numerical results," *IEEE Trans. Med. Imag.*, vol. MI-1, no. 2, pp. 95–101, Oct. 1982.

[19] D. C. Youla, "Generalized image restoration by the method of alternating orthogonal projections," *IEEE Trans. Circuits Syst.*, vol. CAS-25, no. 9, 1978.

[20] H. Stark and P. Oskoui, "High-resolution image recovery from image-plane arrays using convex projections," *Journal of the Optical Society of America A*, vol. 6, no. 11, pp. 1715–1726, Nov. 1989.

[21] A. M. Tekalp, M. K. Ozkan, and M. I. Sezan, "High-resolution image reconstruction from lower-resolution images sequences and space-varying image restoration," *IEEE International Conference on Acoustics, Speech and Signal Processing*, vol. 2, pp. 169–172, March 1992.

[22] M. K. Ozkan, A. M. Tekalp, and M. I. Sezan, "POCS-based restoration of space-varying blurred images," *IEEE Trans. Image Processing*, vol. 3, no. 4, pp. 450–454, July 1994.

[23] Yeh and Stark, "Iterative and one-step reconstruction from nonuniform samples by convex projections," *J. Optical Society of America A*, vol. 7, no. 3, pp. 491–499, March 1990.

[24] D. Granrath and J. Lersch, "Fusion of images on affine sampling grids," *J. Opt. Soc. Am. A*, vol. 15, no. 4, pp. 791–801, April 1998.

[25] M. I. Sezan, "An overview of convex projections theory and its application to image recovery problems," *Ultramicroscopy*, vol. 40, pp. 55–67, 1992.

[26] J. Goodman, *Introduction to Fourier Optics*. McGraw-Hill, 1996.

[27] J. D. Gaskill, *Linear Systems, Fourier Transforms, and Optics*. John Wiley & Sons, 1978.

[28] B. R. Hunt, "Super-resolution of images: Algorithms, principles, performance," *International Journal of Imaging Systems and Technology*, vol. 6, pp. 297–304, 1995.

[29] G. Wolberg, *Digital Image Warping*. IEEE Computer Society Press, 1990.

[30] G. C. Holst, *Sampling, Aliasing, and Data Fidelity for Electronic Imaging Systems, Communications, and Data Acquisition*. SPIE Optical Engineering Press, 1998.

[31] J. F. Moreno and J. Melia, "An optimum interpolation method applied to the resampling of NOAA AVHRR data," *IEEE Trans. Geosci. Remote Sensing*, vol. 32, pp. 131–151, 1994.

[32] K. W. Oleson, S. Sarlin, J. Garrison, S. Smith, J. L. Privette, and W. J. Emery, "Unmixing multiple land-cover type reflectances from coarse spatial resolution satellite data," *Remote Sens. Environ.*, vol. 54, no. 2, pp. 98–112, November 1995.

[33] D. G. Baldwin, W. J. Emery, and P. B. Cheeseman, "Higher resolution earth surface features from repeat moderate resolution satellite imagery," *IEEE Trans. Geosci. Remote Sensing*, vol. 36, no. 1, pp. 244–255, Jan. 1998.

[34] M. R. Banham and A. K. Katsaggelos, "Digital image restoration," *IEEE Signal Processing Mag.*, pp. 24–41, Mar. 1997.

[35] A. E. Galbraith, "Resolution enhancement of multi-look imagery," Ph.D. dissertation, The University of Arizona, 2004.

[36] J. R. G. Townshend, C. O. Justice, C. Gurney, and J. McManus, "The impact of misregistration on change detection," *IEEE Trans. Geosci. Remote Sensing*, vol. 30, no. 5, pp. 1054–1060, Sept. 1992.

[37] X. Dai and S. Khorram, "The effects of image misregistration on the accuracy of remotely sensed change detection," *IEEE Trans. Geosci. Remote Sensing*, vol. 36, no. 5, pp. 1566–1577, Sept. 1998.

[38] J. R. Schott, *Remote Sensing: the Image Chain Approach*. Oxford University Press, 1997.

[39] S. Sandmeier, C. Müller, B. Hosgood, and G. Andreoli, "Sensitivity analysis and quality assessment of laboratory BRDF data," *Remote Sens. Environ.*, no. 64, pp. 176–191, 1998.

Amy E. Galbraith received the B.S. in Electrical and Computer Engineering from the University of Colorado, Boulder, in 1994, and the M.S. and Ph.D. in Electrical and Computer Engineering with a minor in Optical Sciences from the University of Arizona, Tucson, in 1996 and 2004. From 2000 through 2004 she worked in the Remote Sensing Sciences group at Los Alamos National Laboratory on image processing and resampling algorithms for the Multispectral Thermal Imager. Dr. Galbraith is currently a staff member of the Space Data Systems group at Los Alamos National Laboratory, where she is working on signal processing algorithms for a space-based reconfigurable computer.

James Theiler received the Ph.D. in Physics from Caltech in 1987, and subsequently held appointments at UCSD, MIT Lincoln Laboratory, Los Alamos National Laboratory, and the Santa Fe Institute. He joined the Space and Remote Sensing Sciences group at Los Alamos National Laboratory in 1994. His professional interests include image processing, remote sensing, and machine learning.

Kurtis J. Thome received the B.S. degree in meteorology from Texas A&M University, College Station, and the M.S. and Ph.D. degrees in atmospheric sciences from the University of Arizona, Tucson. He is currently an Associate Professor of optical sciences at the University of Arizona, where he is head of the Remote Sensing Group. He has served as a member of the Landsat-7, ASTER, and MODIS science teams. His current research is focused on the vicarious calibration of earth-imaging sensors and related studies in atmospheric remote sensing, radiative transfer, and satellite atmospheric correction.

Richard W. Ziolkowski (ScB'74-M'75-PhD'80) received the Sc.B. degree in physics magna cum laude with honors from Brown University in 1974, the M.S. and Ph.D. degrees in physics from the University of Illinois at Urbana-Champaign in 1975 and 1980, respectively. He was a member of the Engineering Research Division at the Lawrence Livermore National Laboratory from 1981 to 1990 and served as the leader of the Computational Electronics and Electromagnetics Thrust Area for the Engineering Directorate from 1984 to 1990. Prof. Ziolkowski joined the Department of Electrical and Computer Engineering at the University of Arizona as an Associate Professor in 1990, and was promoted to Full Professor in 1996. He is currently serving as the Kenneth Von Behren Chaired Professor. His research interests include the application of new mathematical and numerical methods to linear and nonlinear problems dealing with the interaction of acoustic and electromagnetic waves with complex media, metamaterials, and realistic structures.

Prof. Ziolkowski is a member of Tau Beta Pi, Sigma Xi, Phi Kappa Phi, the Institute of Electrical and Electronics Engineers (IEEE), the American Physical Society, the Optical Society of America, the Acoustical Society of America, and Commissions B (Fields and Waves) and D (Electronics and Photonics) of URSI (International Union of Radio Science). He is an IEEE Fellow. He was an Associate Editor for the IEEE Transactions on Antennas and Propagation from 1993-1998. He served as the Vice Chairman of the 1989 IEEE/AP-S and URSI Symposium in San Jose, and as the Technical Program Chairperson for the 1998 IEEE Conference on Electromagnetic Field Computation in Tucson. He served as a member of the IEEE Antennas and Propagation Society (AP-S) Administrative Committee (ADCOM) from 2000-2002. He was a Co-Guest Editor (with Prof. Nader Engheta) for the October 2003 IEEE Transactions on Antennas and Propagation Special Issue on Metamaterials. He served as the IEEE AP-S Vice President in 2004. He is currently serving as the IEEE AP-S President. For the US URSI Society he served as Secretary for Commission B (Fields and Waves) from 1993-1996 and as Chairperson of the Technical Activities Committee from 1997-1999, and as Secretary for Commission D (Electronics and Photonics) from 2001-2002. He served as a Member-at-Large of the U.S. National Committee (USNC) of URSI from 2000-2002 and is now serving as a member of the International Commission B Technical Activities Board.

For the Optical Society of America he was a Co-Guest Editor (with Prof. Kurt Oughstun) of the 1998 special issue of J. Opt. Soc. Am. A featuring Mathematics and Modeling in Modern Optics. He was a Co-Organizer (with Dr. Brent Little) of the Photonics Nanostructures Special Symposia at the 1998, 1999, 2000 OSA Integrated Photonics Research (IPR) Topical Meetings. He served as the Chair of the IPR sub-committee IV, Nanostructure Photonics, in 2001. He was a Steering Committee Member for the 27th ESA Antenna Technology Workshop on Innovative Periodic Antennas: Electromagnetic Bandgap, Left-handed Materials, Fractal and Frequency Selective Surfaces in Santiago de Compostela, Spain, in March 2004. He served as a co-Chair of the International Advisory Committee for the IEEE International Workshop on Antenna Technology: Small Antennas and Novel Metamaterials, which was held in Singapore in March 2005.

Prof. Ziolkowski was awarded the Tau Beta Pi Professor of the Year Award in 1993 and the IEEE and Eta Kappa Nu Outstanding Teaching Award in 1993 and 1998. He also holds the title of Sensei with a Nidan rank in Matsunoryu Goshin Jujitsu and a Shodan rank in Kajukenbo.